# Neutral Current Interactions in $e^{\pm}p$ Scattering with Longitudinally Polarised Leptons

H1 Collaboration

**Abstract**

The inclusive single differential cross section $d\sigma/dQ^2$ and the reduced double differential cross section $\tilde{\sigma}(x, Q^2)$ are presented for the neutral current process, $e^{\pm}p \to e^{\pm}X$, in interactions with longitudinally polarised lepton beams using the complete HERA-II data set. The cross sections are measured in the region of large negative four-momentum transfer squared $Q^2 \geq 200$ GeV$^2$ and inelasticity $y < 0.9$. The data are consistent with the expected $Q^2$ dependence of polarised cross sections. The data are compared to predictions of the Standard Model which is able to provide a good description of the data. The polarisation asymmetry is measured as a function of $Q^2$ and found to be in agreement with expectation. The cross sections are combined with previously published data from H1 to obtain the most precise unpolarised measurements. These are used to extract the structure function $xF_3^{\gamma Z}$.

# 1 Introduction

HERA measurements of proton structure in neutral current (NC) deep inelastic scattering (DIS) with polarised lepton beams are crucial to the understanding of the detailed dynamics of QCD as well as allowing the chiral structure of electroweak interactions to be simultaneously probed at the highest energies. Previously published measurements [1, 2, 3, 4, 5] have already provided unique constraints [3, 5, 6, 7] on the parton densities functions (PDFs) of the proton as well as the axial and vector couplings of the light quarks to the $Z^0$ boson [8].

First neutral current (NC) cross section measurements of data taken in the second phase of HERA operation with longitudinally polarised leptons beams have been reported [9] for both electron and positron scattering. The data presented here supercede those results, now using the complete HERA-II data set, and are presented here in detail.

In this paper measurements of the inclusive NC single differential cross sections, $\mathrm{d}\sigma/\mathrm{d}Q^2$ and the reduced cross section $\tilde{\sigma}(x, Q^2)$ are presented for $e^+p$ and $e^-p$ scattering. The data were taken with an incident lepton beam energy of $27.5\,\mathrm{GeV}$, whilst the unpolarised proton beam energy was $920\,\mathrm{GeV}$, yielding a centre-of-mass energy of $\sqrt{s} = 318\,\mathrm{GeV}$. Both data sets are further subdivided into samples of left handed and right handed longitudinal polarisation, $P_e = (N_R - N_L)/(N_R + N_L)$, where $N_R$ ($N_L$) is the number of right (left) handed leptons in the beam. The corresponding data sets are termed the $R$ and $L$ data sets respectively. The corresponding luminosity and longitudinal lepton beam polarisation is given in Tab. 1 below.

| | $R$ | $L$ |
|---|---|---|
| $e^-p$ | $\mathcal{L} = 45.9\ \mathrm{pb}^{-1}$<br>$P_e = (+36.9 \pm 2.3)\%$ | $\mathcal{L} = 103.2\ \mathrm{pb}^{-1}$<br>$P_e = (-26.1 \pm 1.0)\%$ |
| $e^+p$ | $\mathcal{L} = 98.1\ \mathrm{pb}^{-1}$<br>$P_e = (+32.5 \pm 1.2)\%$ | $\mathcal{L} = 81.9\ \mathrm{pb}^{-1}$<br>$P_e = (-37.6 \pm 1.4)\%$ |

Table 1: Table of integrated luminosities, $\mathcal{L}$, and luminosity weighted longitudinal polarisation, $P_e$ for the data sets presented here.

# 2 The Neutral Current Cross Section

The generalised proton structure functions, $\tilde{F}_{2,3}$, may be written as linear combinations of the hadronic structure functions $F_2$, $F_{2,3}^{\gamma Z}$, and $F_{2,3}^{Z}$ containing information on QCD parton dynamics as well as the EW couplings of the quarks to the neutral vector bosons. The function $F_2$ is associated to pure photon exchange terms, $F_{2,3}^{\gamma Z}$ correspond to photon-$Z^0$ interference and $F_{2,3}^{Z}$ correspond to the pure $Z^0$ exchange terms. In addition the longitudinal structure function $\tilde{F}_L$ may be similarly decomposed, however this is important only at high $y$ and is expected to be negligible at large $x$ (the familiar Bjorken $x$ variable) and $Q^2$. Neglecting $\tilde{F}_L$, the linear

combinations for arbitrarily polarised $e^{\pm}p$ scattering are given by

$$\tilde{F}_2^{\pm} = F_2 - (v_e \pm P_e a_e)\kappa \frac{Q^2}{Q^2+M_Z^2} F_2^{\gamma Z} + (v_e^2 + a_e^2 \pm P_e 2 v_e a_e)\kappa^2 \left[\frac{Q^2}{Q^2+M_Z^2}\right]^2 F_2^Z \quad (1)$$

$$x\tilde{F}_3^{\pm} = -(a_e \pm P_e v_e)\kappa \frac{Q^2}{Q^2+M_Z^2} x F_3^{\gamma Z} + (2 a_e v_e \pm P_e [v_e^2 + a_e^2])\kappa^2 \left[\frac{Q^2}{Q^2+M_Z^2}\right]^2 x F_3^Z \quad (2)$$

Here $\kappa^{-1} = 4\frac{M_W^2}{M_Z^2}(1-\frac{M_W^2}{M_Z^2})$ in the on-mass-shell scheme [10] with $M_W$ and $M_Z$ the usual weak vector boson masses. For the first time HERA is sensitive to the parity violating terms of the Standard Model, namely those proportional to $P_e$ in eqs. 2 above.

In the quark parton model, the hadronic structure functions are related to linear combinations of sums and differences of the quark and anti-quark momentum distributions $xq(x,Q^2)$ and $x\bar{q}(x,Q^2)$

$$\left[F_2, F_2^{\gamma Z}, F_2^Z\right] = x\sum_q [e_q^2, 2e_q v_q, v_q^2 + a_q^2](q+\bar{q}) \quad (3)$$

$$\left[xF_3^{\gamma Z}, xF3^Z\right] = 2x\sum_q [e_q a_q, v_q a_q](q-\bar{q}) \ , \quad (4)$$

where $v_q$ and $a_q$ are the vector and axial-vector couplings of the light quarks and $e_q$ is the charge of the quark of flavour $q$.

The differential cross section for $e^{\pm}$ scattering after correction for QED radiative effects is then given by

$$\frac{\mathrm{d}^2\sigma_{\mathrm{NC}}^{\pm}}{\mathrm{d}x\mathrm{d}Q^2} = \frac{2\pi\alpha^2}{xQ^4}(Y_+\tilde{F}_2 \mp Y_- x\tilde{F}_3 - y^2\tilde{F}_L) \ , \quad (5)$$

and the reduced cross section is defined by

$$\tilde{\sigma}^{\pm}(x,Q^2) \equiv \frac{\mathrm{d}^2\sigma_{\mathrm{NC}}^{\pm}}{\mathrm{d}x\mathrm{d}Q^2}\frac{xQ^4}{2\pi\alpha^2}\frac{1}{Y_+} \equiv \tilde{F}_2 \mp \frac{Y_-}{Y_+}x\tilde{F}_3 - \frac{y^2}{Y_+}\tilde{F}_L \ . \quad (6)$$

The helicity dependence of the electroweak interactions is contained within the terms $Y_{\pm} = 1 \pm (1-y^2)$ where $y$ characterises the inelasticity of the interaction.

# 3 Experimental Technique

The H1 detector components most relevant to this analysis are the liquid argon (LAr) calorimeter, which measures the positions and energies of charged and neutral particles over the polar[1] angular range $4^\circ < \theta < 154^\circ$, and the inner tracking detectors, which measure the angles and momenta of charged particles over the range $7^\circ < \theta < 165^\circ$. A full description of the detector can be found in [11].

[1]The polar angle $\theta$ is defined with respect to the positive $z$ axis, the direction of the incident proton beam.

The $ep$ luminosity is determined by measuring the QED bremsstrahlung ($ep \to ep\gamma$) event rate by tagging the low angle scattered lepton in a detector located at $z = -44$m adjacent to the beam pipe.

At HERA transverse polarisation of the lepton beam arises naturally through synchrotron radiation via the Sokolov-Ternov effect [12]. In $2000$ a pair of spin rotators was installed in the beamline on either side of the H1 detector, allowing transversely polarised leptons to be rotated into longitudinally polarised states and back again. The degree of polarisation is constant around the HERA ring and is continuously measured using two independent polarimeters LPOL [13] and TPOL [14]. The polarimeters are situated in beamline sections in which the beam leptons have longitudinal and transverse polarisations respectively. Both measurements rely on an asymmetry in the energy spectrum of left and right handed circularly polarised photons undergoing Compton scattering with the lepton beam. The TPOL measurement uses in addition a spatial asymmetry. The LPOL polarimeter measurements are used when available and TPOL measurements otherwise. The polarisation profile weighted by the luminosity values is shown in Fig. 1(a) and (b) for the $e^+$ and $e^-$ samples respectively.

Simulated DIS events are used in order to determine acceptance corrections. DIS processes are generated using the DJANGO [15] Monte Carlo (MC) simulation program, which is based on LEPTO [16] for the hard interaction and HERACLES [17] for single photon emission and virtual EW corrections. LEPTO combines $\mathcal{O}(\alpha_s)$ matrix elements with higher order QCD effects using the colour dipole model as implemented in ARIADNE [18]. The JETSET program [19] is used to simulate the hadronisation process. In the event generation the DIS cross section is calculated using the H1 PDF $2009$ [3] parametrisation for the proton PDFs.

The dominant $ep$ background contribution arises from photoproduction processes. These are simulated using the PYTHIA [20] MC with leading order PDFs for the proton taken from CTEQ [21] and for the photon from GRV [22]. Further backgrounds from NC DIS, QED-Compton scattering, lepton pair production, prompt photon production and heavy gauge boson ($W^{\pm}$, $Z^0$) production are also simulated; their final contribution to the analysis sample is small. Further details are given in [3].

The detector response to events produced by the generation programs is simulated in detail using a program based on GEANT [23]. These simulated events are then subjected to the same reconstruction and analysis chain as the data.

The selection of candidate NC events follows closely that of the previously published analysis of unpolarised data from H1 [3] and is briefly described below.

NC events are characterised by an isolated high transverse momentum lepton and a hadronic system opposite in azimuth to the scattered lepton. Such events are triggered mainly using information from the LAr calorimeter. The calorimeter has finely segmented geometry allowing the selection of localised energy deposits in the electromagnetic sections of the calorimeter. This selection is found to be $100\%$ efficient for leptons above $11$ GeV.

The hadronic final state particles are reconstructed using a combination of tracks and calorimeter deposits in an energy flow algorithm that avoids double counting [24, 25].

The NC sample is used to carry out an *in-situ* calibration of the electromagnetic and hadronic energy scales of the LAr calorimeter using the method described in [3, 24, 25]. The hadronic

calibration procedure is based on the double angle reconstruction method [26] which uses the polar angles of the scattered lepton and the hadronic final state to determine their respective energies. The calibration procedure gives good agreement between data and simulation within an estimated uncertainty of $2\%$ on the hadronic scale and between $1-3\%$ on the electromagnetic scale.

The NC kinematic quantities are determined using the $e\Sigma$ method [27] which uses information from the scattered lepton and the hadronic final state optimising kinematic resolution and minimising QED radiative corrections across the measured kinematic plane.

# 4 Measurement Procedure

Candidate NC interactions are selected by requiring the scattered lepton energy $E'_e > 11\,\mathrm{GeV}$, $Q^2_e > 133$ GeV$^2$ and a reconstructed vertex within $35\,\mathrm{cm}$ in $z$ of the nominal interaction point. Background from misidentified leptons is suppressed by requiring a charged track to be associated to the lepton candidate. Longitudinal energy-momentum conservation requires that $E - P_z = 2E_e$ where $E_e$ is the lepton beam energy and $E$ and $P_z$ are the usual components of the hadronic final state four-vector. By requiring $E - P_z > 35$ GeV the influence of radiative corrections is considerably reduced which arises from initial state bremmsstrahlung. This requirement further suppresses the contamination from photoproduction background in which the the scattered lepton is undetected in the backward beam pipe and a hadron is misidentified as a lepton candidate.

The comparison of the data and the simulation (normalised to the luminosity of the data) is shown in Fig. 2 for the distribution of scattered lepton energy $E'_e$, the lepton polar angle $\theta_e$, the reconstructed $Q^2_e$, and the transverse momentum balance between the lepton and the hadronic final state, $P^h_T/P^e_T$. The left and right handed samples are combined in these figures. In all cases the simulation provides an accurate description of the data and is used to correct for selection and resolution effects.

The systematic uncertainties on the cross section measurements are discussed briefly below (see [24, 25] and references therein for more details). Positive and negative variations of one standard deviation of each error source are found to yield errors which are symmetric to a good approximation. The systematic uncertainties of each source are taken to be fully uncorrelated between the cross section measurements unless stated otherwise.

- An uncertainty of $1\%$ ($z_{imp} < +20\mathrm{cm}$), $2\%$ ($+20\mathrm{cm} < z_{imp} < +100\mathrm{cm}$) and $3\%$ for $z_{imp} > +100\mathrm{cm}$) is assigned to the scale of the electromagnetic energy measured in the LAr calorimeter, where $z_{imp}$ is the z co-ordinate of the impact position of the scattered lepton in the LAr calorimeter. $0.5\%$ of this uncertainty is considered as a correlated component.

- An uncertainty of $0.5\%$ for $\theta_e < 100^\circ$ and $2\%$ for $\theta_e > 100^\circ$ in the identification of the scattered electron or positron.

- An uncertainty in the polar angle measurement of the scattered lepton is taken to be $2$ mrad for $\theta_e > 120^\circ$ and $3$ mrad elsewhere.

- An uncertainty of $2\%$ is assigned to the scale of the hadronic energy measured in the detector, of which $1\%$ is considered as a correlated component to the uncertainty.
- A $10\%$ correlated uncertainty is assigned to the amount of energy in the LAr calorimeter attributed to noise.
- A 1% uncertainty on the trigger efficiency.
- A $30\%$ correlated uncertainty on the subtracted $ep$ background is determined from a comparison of data and simulation after relaxing the anti-photoproduction cuts, such that the sample is dominated by photoproduction events.
- The combined uncertainty of finding an interaction vertex and associating a track to the scattered lepton is estimated to be $3\%$ for the $e^+p$ data and $2\%$ for the $e^-p$ data uncorrelated from point to point.
- An uncertainty of $0.5\%$ accounts for the dependence of the acceptance correction on the PDFs used in the MC simulation.
- An error of $1\%$ is estimated for the QED radiative corrections. This accounts for missing contributions in the simulation of the lowest order QED effects and for the uncertainty on the higher order QED and EW corrections.
- An uncertainty of $z$ dependence of the proton bunch structure is estimated to be $0.5\%$.
- The relative uncertainty in the measurement of the lepton beam polarisation is taken to be $1.6\%$ for the LPOL and $3.5\%$ for the TPOL [28], yielding a total relative polarisation uncertainty in the $e^+p$ sample of $1.2\%$ for the $R$ data set and $1.4\%$ for the $L$ data set. For the $e^-p$ data a relative uncertainty of $2.3\%$ for the $R$ data set and $1.0\%$ for the $L$ data set is obtained. These uncertainties are not included in the error bars of the data points.
- In addition, there is a global uncertainty of $2.1\%$ on the luminosity measurement for both the $R$ and $L$ $e^{\pm}p$ data samples.

The total systematic error is formed by adding the individual uncertainties in quadrature.

# 5 Results

The measured cross sections $\frac{\mathrm{d}\sigma}{\mathrm{d}Q^2}$ for $y < 0.9$ are shown in Figs. 3 and 5 for $e^+p$ and $e^-p$ scattering respectively. The data are measured in the range $Q^2 \geq 200$ GeV$^2$ up to $Q^2 \simeq 20\,000$ GeV$^2$ over which the cross sections fall by almost six orders of magnitude with increasing $Q^2$. The cross sections are found to be similar at low $Q^2$ for both lepton charges and polarisations, however at the highest $Q^2$ differences are observed between the $e^+p$ and $e^-p$ cross sections arising from the structure function $x\tilde{F}_3$. The data from both polarised samples are combined together and corrected for the remaining residual polarisation to provide a measurement of the unpolarised cross sections. These are shown in Figs. 4 and 6.

The measured data are compared to the Standard Model expectation from the H1 PDF 2009 fit [5] which provides an excellent description of the $Q^2$ dependence of the data including the difference between the $e^+p$ and $e^-p$ cross sections.

The comparisons of the measured unpolarised single differential cross sections to various Standard Model predictions using different sets of PDFs are shown in Figs. 7 and 8. It can be seen that the H1 PDF 2009 expectations reproduce the shape of the steeply falling cross sections very well for both $e^-p$ and $e^+p$ scattering. However, the prediction is approximately $3-4\%$ larger than the measurements as shown in Figs. 7 and 8(a). The total correlated normalisation uncertainty is shown as dashed blue line on the inset figures and is $\pm 2.1\%$. Comparisons to Standard Model expectations using the HERAPDF1.0 set of PDFs are shown in Figs. 7 and 8(b) and are able to accurately describe both shape and normalisation of the cross sections in $e^-p$ and $e^+p$ scattering. Also shown are the predictions using the CTEQ6m PDFs which predict approximately $3-4\%$ smaller cross sections than are measured. At the very highest $Q^2$ the $e^-p$ measurements have a tendency to overshoot the predictions albeit with large statistical uncertainties.

In order to improve the statistical precision of the measurements these cross sections are combined with previoulsy published HERA-I measurements from H1 [1, 2, 3] using the statistical combination procedure described in detail in [4]. This method forms a model independant average from several measurements of the same cross section taking into account the systematic uncertainties correlated across the data sets. The final combined cross sections make use of the complete HERA dataset collected by H1 and amounts to a total luminosity of $165.5$ pb$^{-1}$ for $e^-p$ scattering and $280.8$ pb$^{-1}$ for $e^+p$ scattering. The combined cross sections are shown in Figs. 11 and 12 where again it can be seen that the expectation from H1 PDF 2009 is approxmimately $2-3\%$ larger than the combined measurements and the CTEQ6m PDFs predict a cross section approximately $2-3\%$ lower than the measurements whereas the HERAPDF1.0 PDFs provide a very good description of the shape and normalisation of the cross sections.

The Standard Model also predicts a difference in the cross section for leptons with different helicity states arising from the chiral structure of the neutral electroweak exchange. With longitudinally polarised lepton beams in HERA-II such polarisation effects can be tested, providing a direct measure of electroweak effects in the neutral current cross sections. The polarisation asymmetry, $A$, is defined as

$$A = \frac{2}{P_R - P_L} \cdot \frac{\sigma^{\pm}(P_R) - \sigma^{\pm}(P_L)}{\sigma^{\pm}(P_R) + \sigma^{\pm}(P_L)} \ . \tag{7}$$

To a very good approximation $A$ measures the structure function ratio

$$A^{\pm} \simeq \mp k a_e \frac{F_2^{\gamma Z}}{F_2} \tag{8}$$

which is proportional to combinations $a_e v_q$ and is thus a direct measure of parity violation. In positron scattering $A$ is expected to be positive and about equal to $-A$ in electron scattering. At large $x$ the asymmetry measures the $d/u$ ratio of the valence quark distributions according to

$$A^{\pm} \simeq \pm k \frac{1 + d_v/u_v}{4 + d_v/u_v}. \tag{9}$$

The polarised single differential cross sections $\mathrm{d}\sigma/\mathrm{d}Q^2$ from HERA-II are used to construct the asymmetry where it is assumed that the correlated uncertainties of each measurement cancel. The asymmetry is shown in Fig. 13 compared to the Standard Model expectation from H1 PDF 2009. The magnitude of the asymmetry is observed to increase with increasing $Q^2$ and is negative in $e^-p$ and positive in $e+p$ scattering. The data are in good agreement with the Standard Model expectation using H1 PDF 2009 and confirm the violation of parity in the neutral current channel.

The measurements are also presented as double differential reduced cross sections, $\tilde{\sigma}_{NC}(x, Q^2)$ for $e^-p$ and $e^+p$ scattering in Figs. 14 and 15 respectively. The cross sections are measured over the $Q^2$ range $150$ to $30\,000$ GeV$^2$ and over the $x$ range $0.0032$ to $0.65$. The cross sections have a typical precision of $3\%$ for $Q^2 < 1\,000$ GeV$^2$ and are statistically limited at higher $Q^2$. In $e^-p$ scattering the $L$ sample yeilds a cross section that is enhanced with respect to the $R$ sample whereas the reverse is true in $e^+p$ data. The H1 PDF 2009 prediction describes the $x$ dependance of the measured cross sections well.

In Fig. 16 the polarised reduced cross section measurements are combined to produce an unpolarised measurement corrected for the residual polarisation. These cross sections are shown in Fig. 16 for $e^{\pm}p$ scattering. At low $Q^2$ the two measurements are consistent with one another, however as the $Q^2$ increases toward and beyond the Electroweak scale a clearly increasing discrepancy between the $e^-p$ and $e^+p$ cross sections is observed, consistent with the Standard Model expectation. Positron scattering is suppressed with respect to electron scattering through the increasing contribution of the structure function $x\tilde{F}_3$.

In order to improve precision the double differential cross section measurements are combined with previously published measurements from HERA-I [1, 2, 3] using the same method as described in [4]. The combined double differential cross sections can be seen in Fig. 17 for the $Q^2$ range above $150$ GeV$^2$. Again the, influence of $Z^0$ is clearly visible and is shown for $Q^2 > 1\,000$ GeV$^2$ in Fig.18.

The structure functions $x\tilde{F}_3$ may be obtained using the equation

$$x\tilde{F}_3 = \frac{Y_+}{2Y_-}\left[\tilde{\sigma}^-(x, Q^2) - \tilde{\sigma}^+(x, Q^2)\right] \tag{10}$$

and is shown in Fig. 19 for all measured $x,\ Q^2$ bins. In the context of the Standard Model it can be seen from Eq. 2 that the dominant contribution to $x\tilde{F}_3$ arises from the $\gamma Z$ interference term, since the pure $Z$ exchange term is suppresed by an additional factor of $\kappa Q^2/(Q^2 + M_Z^2)$ and, in the case of unpolarised scattering, the small vector coupling $v_e$. Thus $x\tilde{F}_3^{\gamma Z}$ may be determined using the approximation

$$xF_3^{\gamma Z} \simeq x\tilde{F}_3 \frac{(Q^2 + M_Z^2)}{a_e \kappa Q^2} \tag{11}$$

neglecting terms proportional to $v_e$. The data are shown in Fig. 20 for the region of $x$ and $Q^2$ where the expected sensitivity is larger than the normalisation uncertainty of the data.

This non-singlet structure function has a weak $Q^2$ dependence and is also shown from the H1 PDF 2000 fit. Since the dependence is weak, the data from each $Q^2$ are transformed to one $Q^2$ value at $1\,500$ GeV$^2$ and then averaged. The combination of extracted $xF_3^{\gamma Z}$ data for all $Q^2$ values is shown in Fig. 21 and is directly sensitive to the valence quark distributions. The Standard Model prediction is also shown and found to be in excellent agreement in both shape and magnitude with the data.

# 6 Summary

The NC cross sections $\mathrm{d}\sigma/\mathrm{d}Q^2$ have been measured for $e^{\pm}p$ scattering with longitudinally polarised lepton beams at HERA. The polarisation asymmetry is measured and data are found to be consistent with the predicted behaviour of the polarised $ep$ scattering in the Standard Model. The cross sections are combined with earlier published H1 measurements using the complete HERA data set.

The double differential NC cross sections $\tilde{\sigma}^{\pm}(x, Q^2)$ have been measured at high $Q^2$ for $e^{\pm}p$ scattering. The data are combined with existing H1 measurements yielding H1 unpolarised cross section measurements using the entire HERA I+II data set. An extraction of the structure functions $x\tilde{F}_3$ and $xF_3^{\gamma Z}$ has been performed. The data are in good agreement with expectation of the Standard Model.

# Acknowledgements

We are grateful to the HERA machine group whose outstanding efforts have made this experiment possible. We thank the engineers and technicians for their work in constructing and maintaining the H1 detector, our funding agencies for financial support, the DESY technical staff for continual assistance and the DESY directorate for support and for the hospitality which they extend to the non DESY members of the collaboration.

# References


[1] C. Adloff *et al.* [H1 Collaboration], Eur. Phys. J. C **13**, 609 (2000) [arXiv:hep-ex/9908059].

[2] C. Adloff *et al.* [H1 Collaboration], Eur. Phys. J. C **19**, 269 (2001) [arXiv:hep-ex/0012052].

[3] C. Adloff *et al.* [H1 Collaboration], Eur. Phys. J. C **30** (2003) 1 [hep-ex/0304003].

[4] H. Collaboration, Eur. Phys. J. C **63** (2009) 625 [arXiv:0904.0929 [hep-ex]].

[5] F. D. Aaron *et al.* [H1 Collaboration], Eur. Phys. J. C **64** (2009) 561 [arXiv:0904.3513 [hep-ex]].

[6] D. Stump, J. Huston, J. Pumplin, W.K. Tung, H.L. Lai, S. Kuhlmann and J.F. Owens, JHEP **0310** (2003) 046 [arXiv:hep-ph/0303013].

[7] A. D. Martin, W. J. Stirling, R. S. Thorne and G. Watt, Eur. Phys. J. C **63** (2009) 189 [arXiv:0901.0002 [hep-ph]].

[8] A. Aktas *et al.* [H1 Collaboration], Phys. Lett. B **632** (2006) 35 [hep-ex/0507080].

[9] A. Nikiforov, "Neutral Current in polarised $e^{\pm}p$ collisions at HERA-II", presented on behalf of the H1 Collaboration at XIVth International Workshop on Deep Inelastic Scattering, Tsukuba, Japan, April 2006

[10] A. Sirlin, Phys. Rev. D **22**, 971 (1980).; A. Sirlin, Phys. Rev. D **29**, 89 (1984).

[11] I. Abt *et al.* [H1 Collaboration], Nucl. Instrum. Meth. A **386** (1997) 310 and 348;
R.D. Appuhn *et al.* [H1 SPACAL Group], Nucl. Instrum. Meth. A **386** (1997) 397.

[12] A.A. Sokolov and I.M. Ternov, Sov. Phys. Dokl. **8** No. 12 (1964) 1203.

[13] M. Beckmann *et al.*, Nucl. Instrum. Meth. A **479** (2002) 334.

[14] D.P. Barber *et al.*, Nucl. Instrum. Meth. A **329** (1993) 79.

[15] G.A. Schuler and H. Spiesberger, Proceedings of the Workshop "Physics at HERA", vol. 3, eds. W. Buchmüller, G. Ingelman, DESY (1992) 1419.

[16] G. Ingelman, Proceedings of the Workshop "Physics at HERA", vol. 3,
eds. W. Buchmüller, G. Ingelman, DESY (1992) 1366.

[17] A. Kwiatkowski, H. Spiesberger and H.-J. Möhring, Comput. Phys. Commun. **69** (1992) 155.

[18] L. Lönnblad, Comput. Phys. Commun. **71** (1992) 15.

[19] T. Sjöstrand and M. Bengtsson, Comput. Phys. Commun. **43** (1987) 367.

[20] T. Sjöstrand, Comput. Phys. Commun. **82** (1994) 74.

[21] H.L. Lai *et al.* [CTEQ Collaboration], Eur. Phys. J. C **12** (2000) 375 [hep-ph/9903282].

[22] M. Glück, E. Reya and A. Vogt, Phys. Rev. D **46** (1992) 1973.

[23] R. Brun *et al.*, GEANT3 User's Guide, CERN-DD/EE-84-1 (1987).

[24] B. Portheault, Ph.D. thesis (March 2005), LAL 05-05 (IN2P3/CNRS), Université de Paris-Sud XI, Orsay, available at http://www-h1.desy.de/publications/theses_list.html.

[25] A. Nikiforov, Ph.D. thesis (June 2007) , Max-Planck-Institut für Physik, Munich, available at http://www-h1.desy.de/publications/theses_list.html.

[26] S. Bentvelsen et.al., Prceedings of the Workshop "Physics at HERA", vol.1, eds. W. Buchmüller, G. Ingelman, DESY (1992) 23; C. Hoeger, ibid, 43.

[27] U. Bassler and G. Bernardi, Nucl. Instrum. Meth. A **361** (1995) 197 [arXiv:hep-ex/9412004]. U. Bassler and G. Bernardi, Nucl. Instrum. Meth. A **426** (1999) 583 [arXiv:hep-ex/9801017].

[28] W. Lorenzon [HERMES Collaboration], DESY-HERMES-97-68, *7th International Workshop on Polarized Gas Targets and Polarized Beams*, Urbana, IL, 18-22 Aug 1997; F. Corriveau *et al.* [TPOL Polarimeter Group], "A Calibration of the HERA Transverse Polarimeter for the 2003/2004 Data", available at http://www.desy.de/∼pol2000/documents/documents.html.

[29] E. Rizvi and T. Sloan, Eur.Phys.J.C direct, **3** (2001) N2 [hep-ex/0101007].

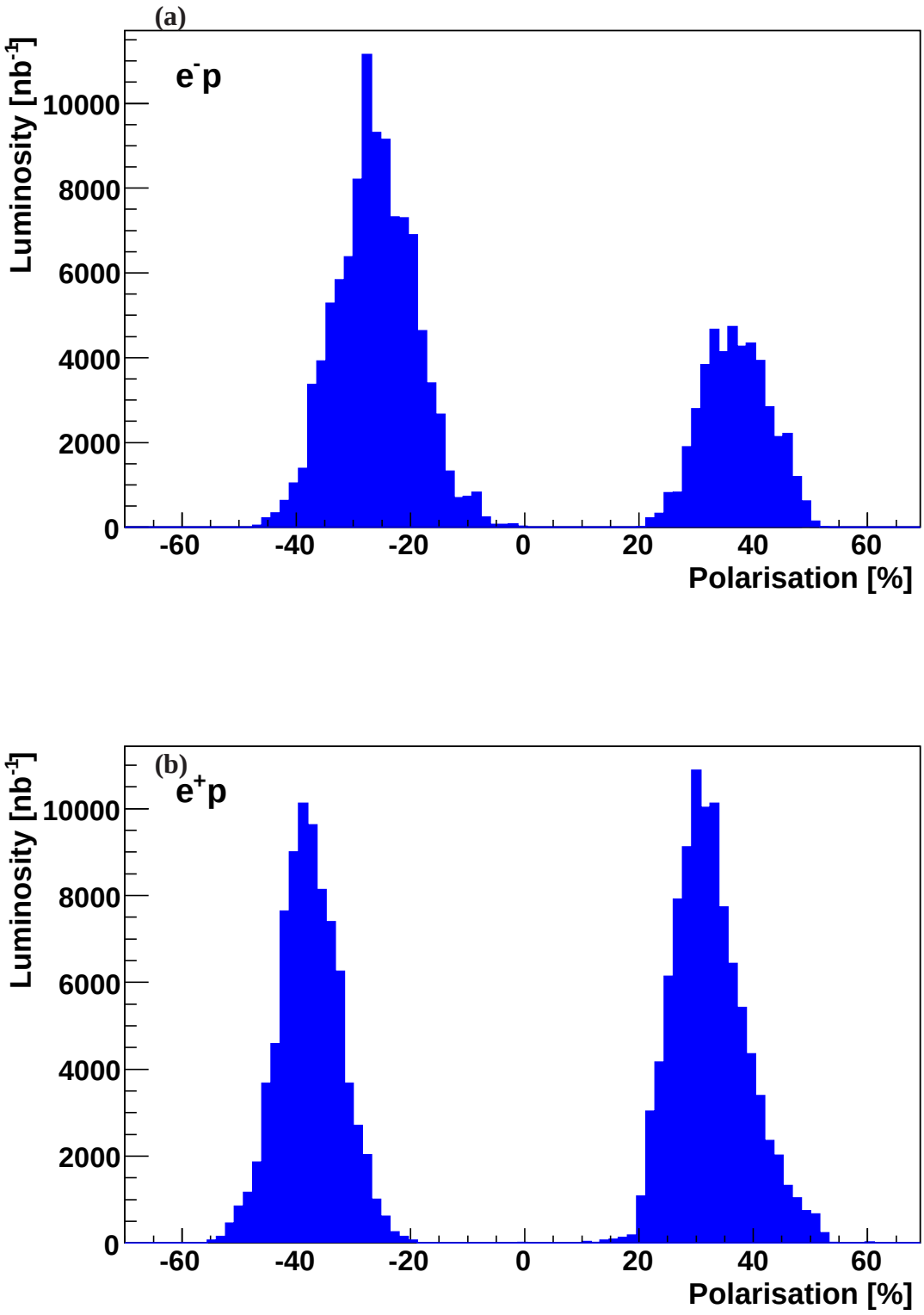


Figure 1: The polarisation profile weighted by the luminosity values for the (a) $e^{-}p$ data and (b) $e^{+}p$ data. The $L(R)$ sample corresponds to distribution having negative (positive) polarisation values.

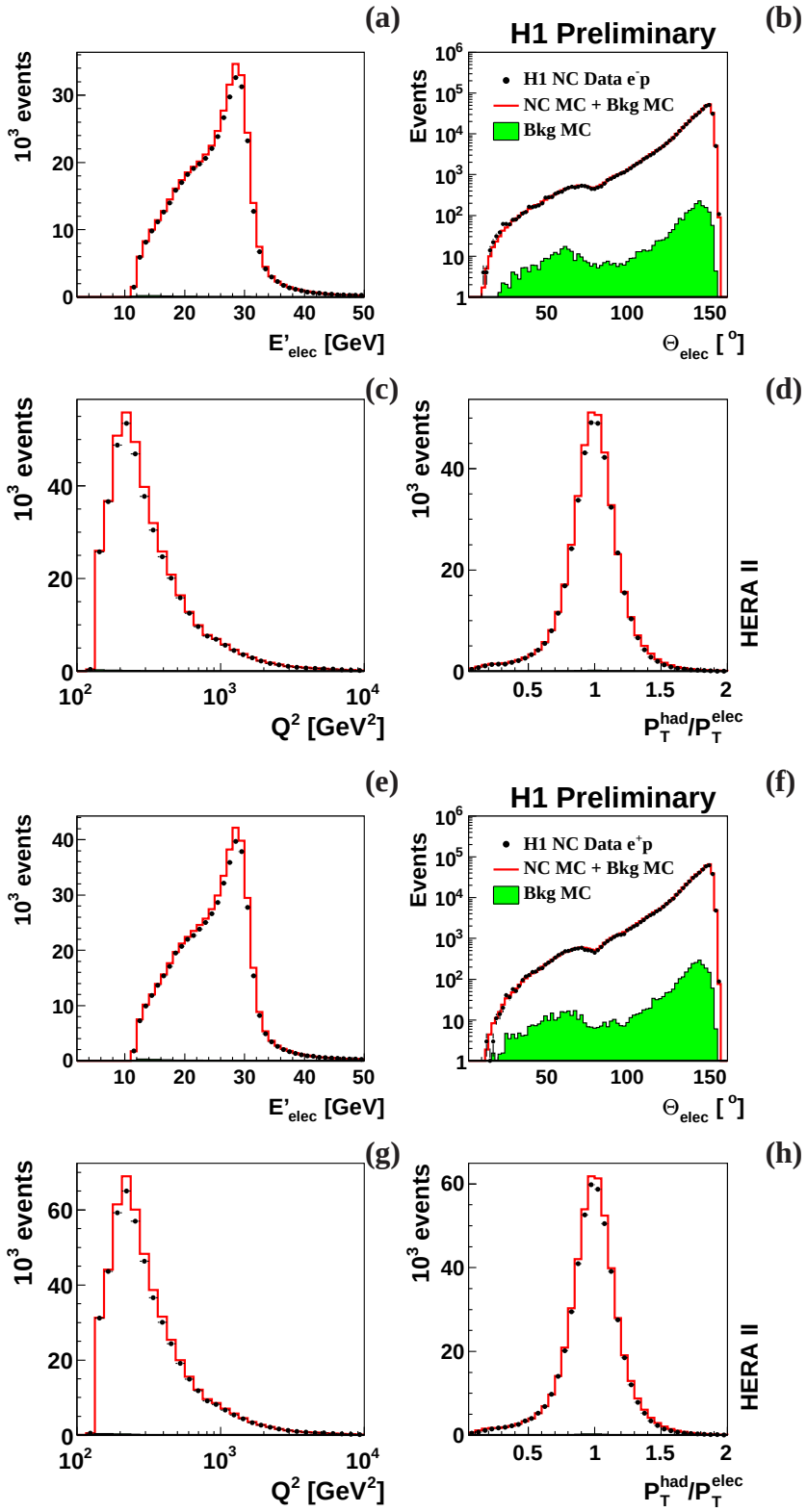


Figure 2: Distributions of (a,e) $E'_e$, (b,f) $\theta_e$, (c,g) $Q^2_e$ and (d,h) $P_{T,h}/P_{T,e}$ shown in upper and lower plots for the selected events in the (a-d) $e^-p$ and (e-h) $e^+p$ data sets. The Monte Carlo (MC) contributions from the neutral current (NC) process and the $ep$ background (bkg) processes are shown as open histograms with the latter contribution alone being shown as shaded histograms. In these plots the left and right handed samples are combined for each lepton charge.

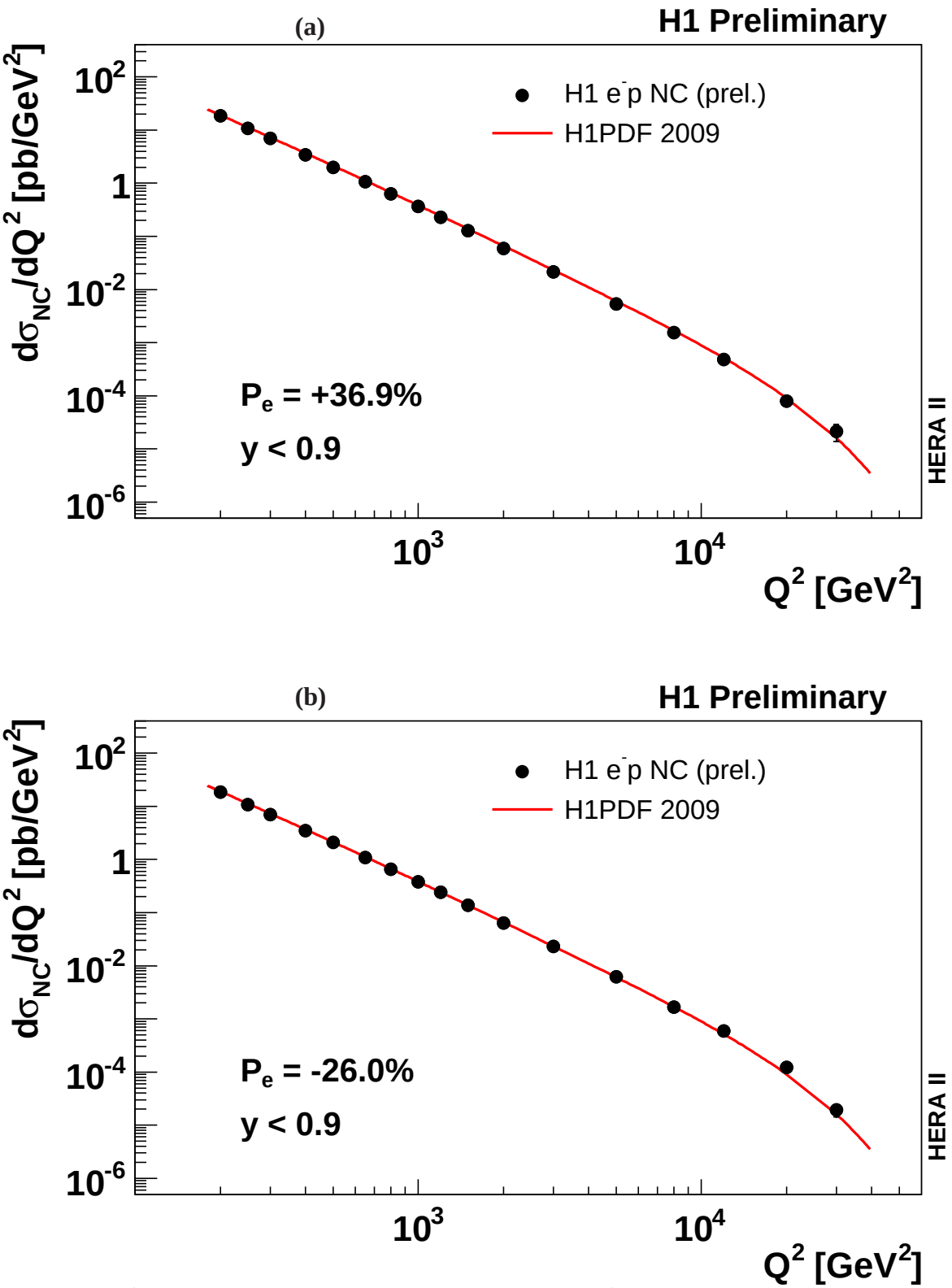


Figure 3: The $Q^2$ dependence of the NC cross section $\mathrm{d}\sigma/\mathrm{d}Q^2$ for $e^-p$ scattering with the (a) right handed $(R)$ and (b) left handed $(L)$ polarisation data sets. The data (solid points) are compared to the Standard Model prediction.

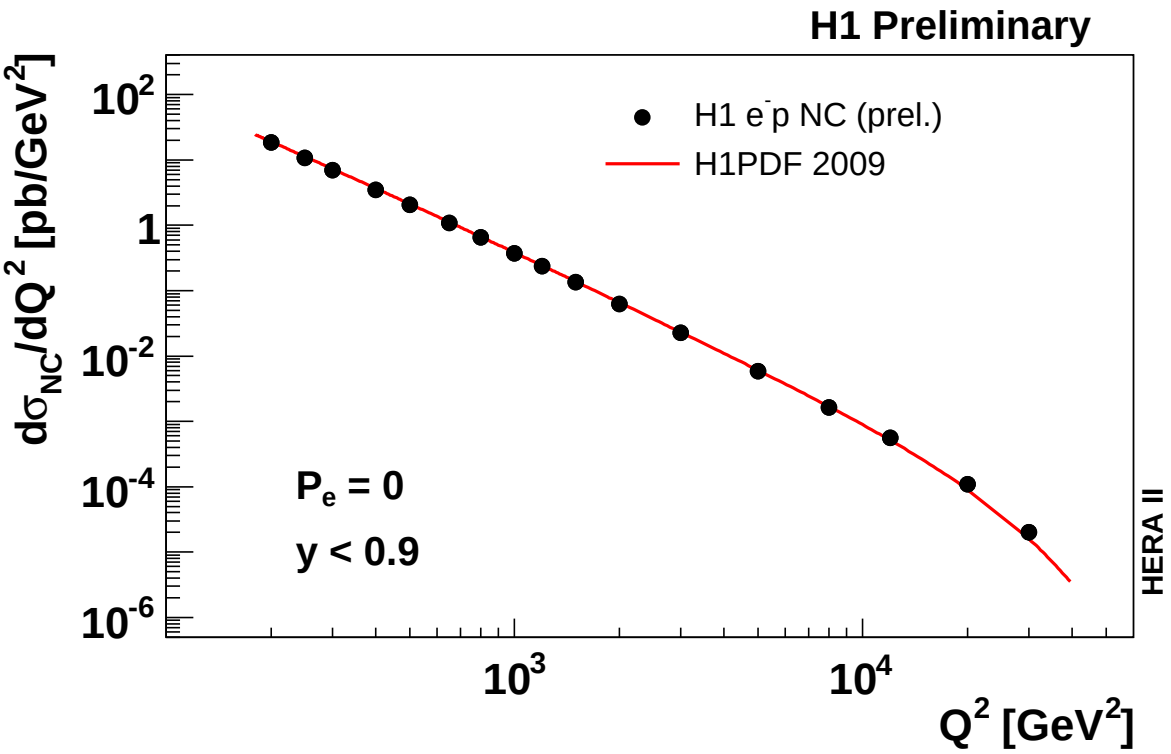


Figure 4: The $Q^2$ dependence of the NC cross section $\mathrm{d}\sigma/\mathrm{d}Q^2$ for $e^-p$ unpolarised scattering. The data (solid points) are compared to the Standard Model prediction.

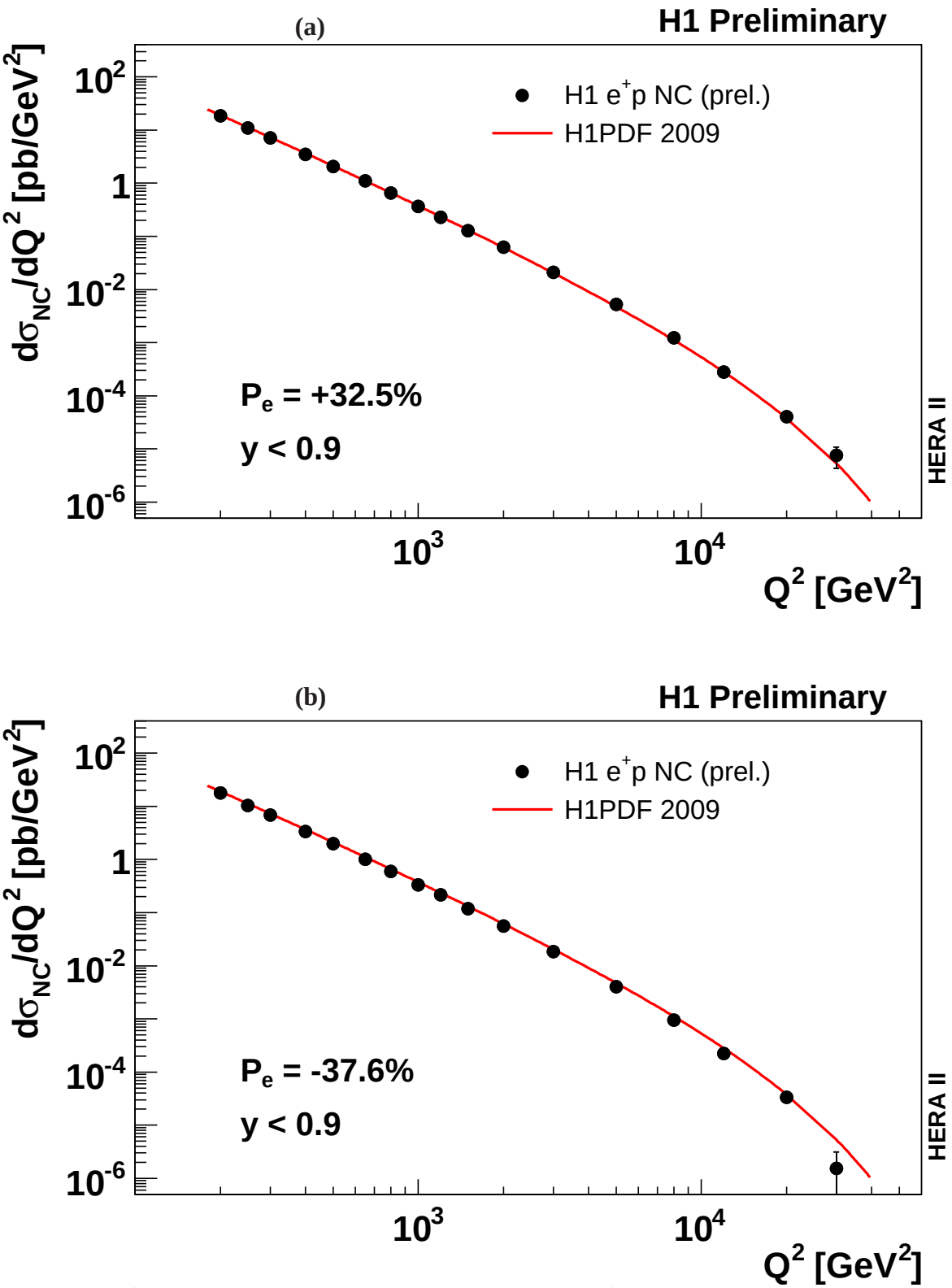


Figure 5: The $Q^2$ dependence of the NC cross section $\mathrm{d}\sigma/\mathrm{d}Q^2$ for $e^+p$ scattering with the (a) right handed $(R)$ and (b) left handed $(L)$ polarisation data sets. The data (solid points) are compared to the Standard Model prediction.

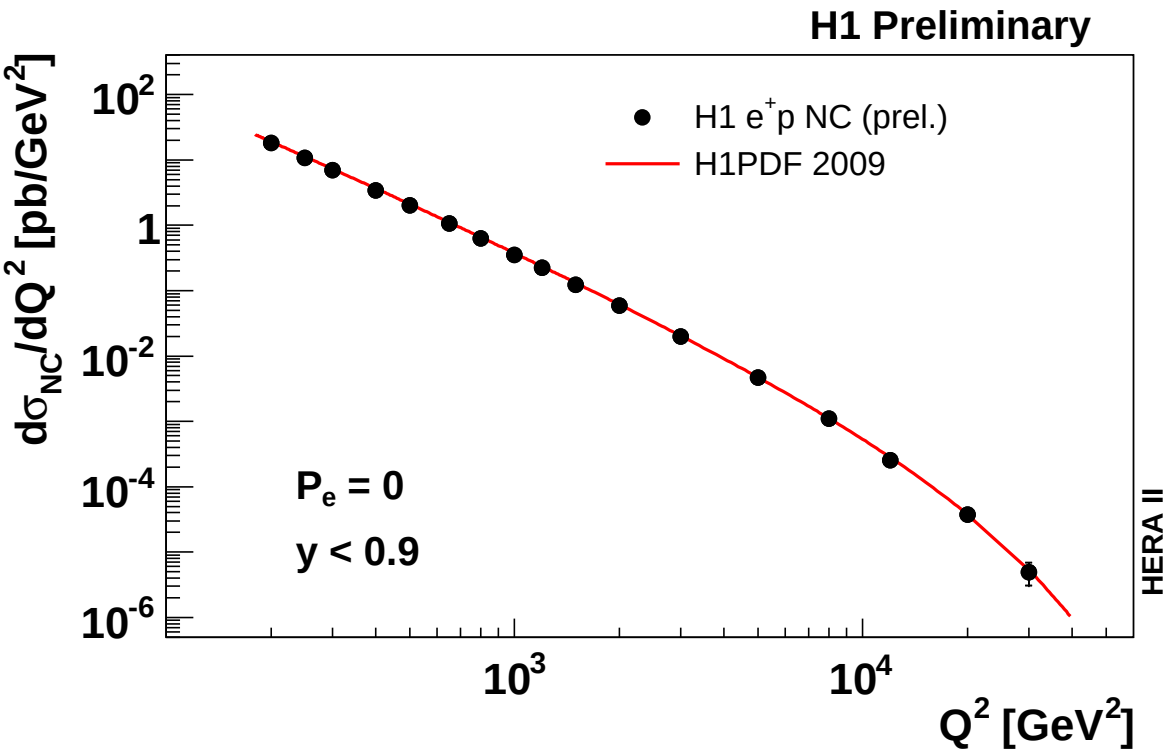


Figure 6: The $Q^2$ dependence of the NC cross section $\mathrm{d}\sigma/\mathrm{d}Q^2$ for $e^+p$ unpolarised scattering. The data (solid points) are compared to the Standard Model prediction.

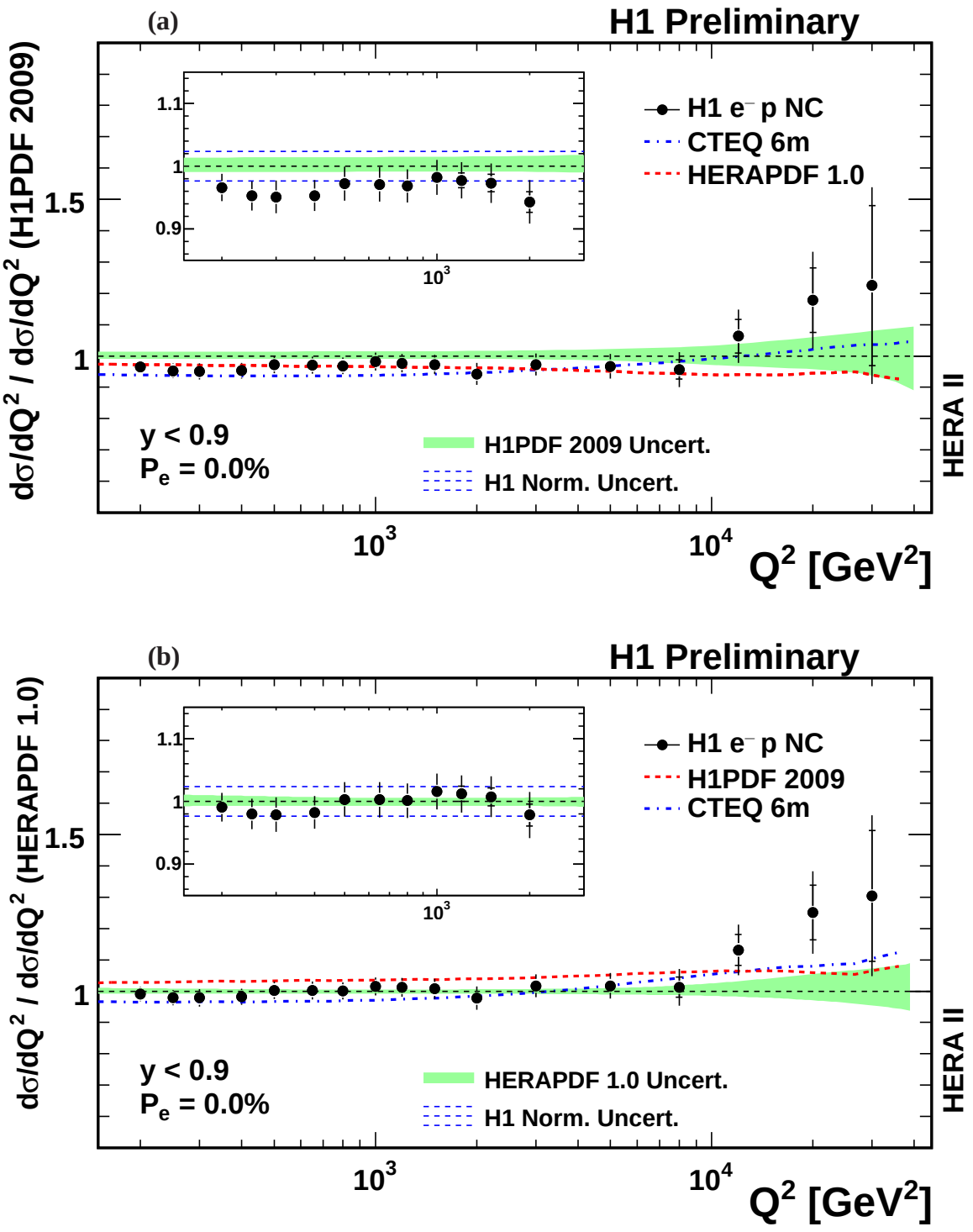


Figure 7: The $Q^2$ dependences of the unpolarised NC cross section ratio $\mathrm{d}\sigma/\mathrm{d}Q^2$ for $e^-p$ scattering using PDFs obtained from (a) H1 PDF 2009 and (b) HERAPDF1.0. In addition the comparisons using CTEQ6m PDFs are also indicated. The data (solid points) are compared to the Standard Model prediction (green band). The inner error bars represent the statistical uncertainties and the outer error bars represent the total errors. The normalisation uncertainty is not included in the error bars and is instead represented by the blue dashed lines on the inset figures.

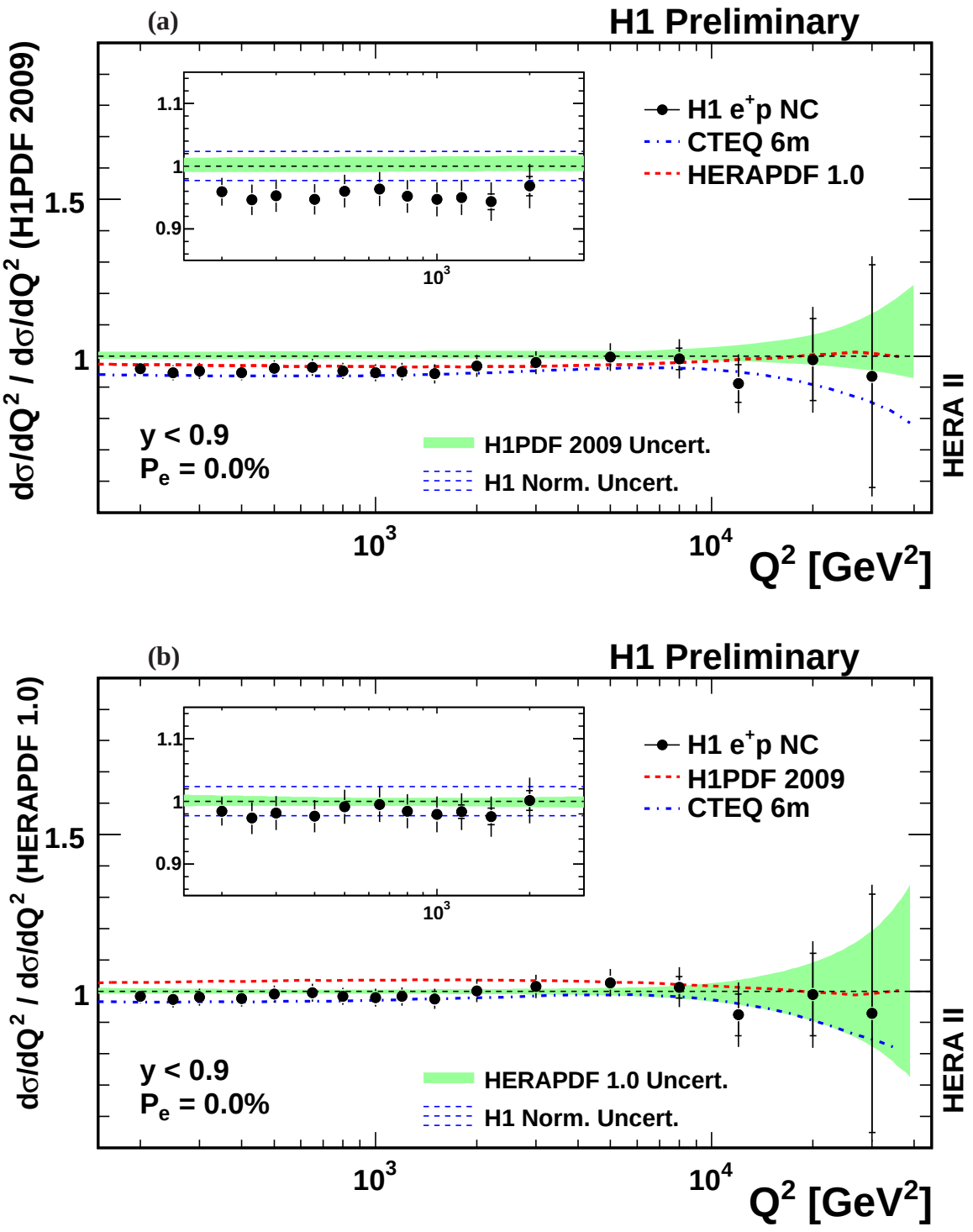


Figure 8: The $Q^2$ dependences of the unpolarised NC cross section ratio $\mathrm{d}\sigma/\mathrm{d}Q^2$ for $e^+p$ scattering using PDFs obtained from (a) H1 PDF 2009 and (b) HERAPDF1.0. In addition the comparisons using CTEQ6m PDFs are also indicated. The data (solid points) are compared to the Standard Model prediction (green band). The inner error bars represent the statistical uncertainties and the outer error bars represent the total errors. The normalisation uncertainty is not included in the error bars and is instead represented by the blue dashed lines on the inset figures.

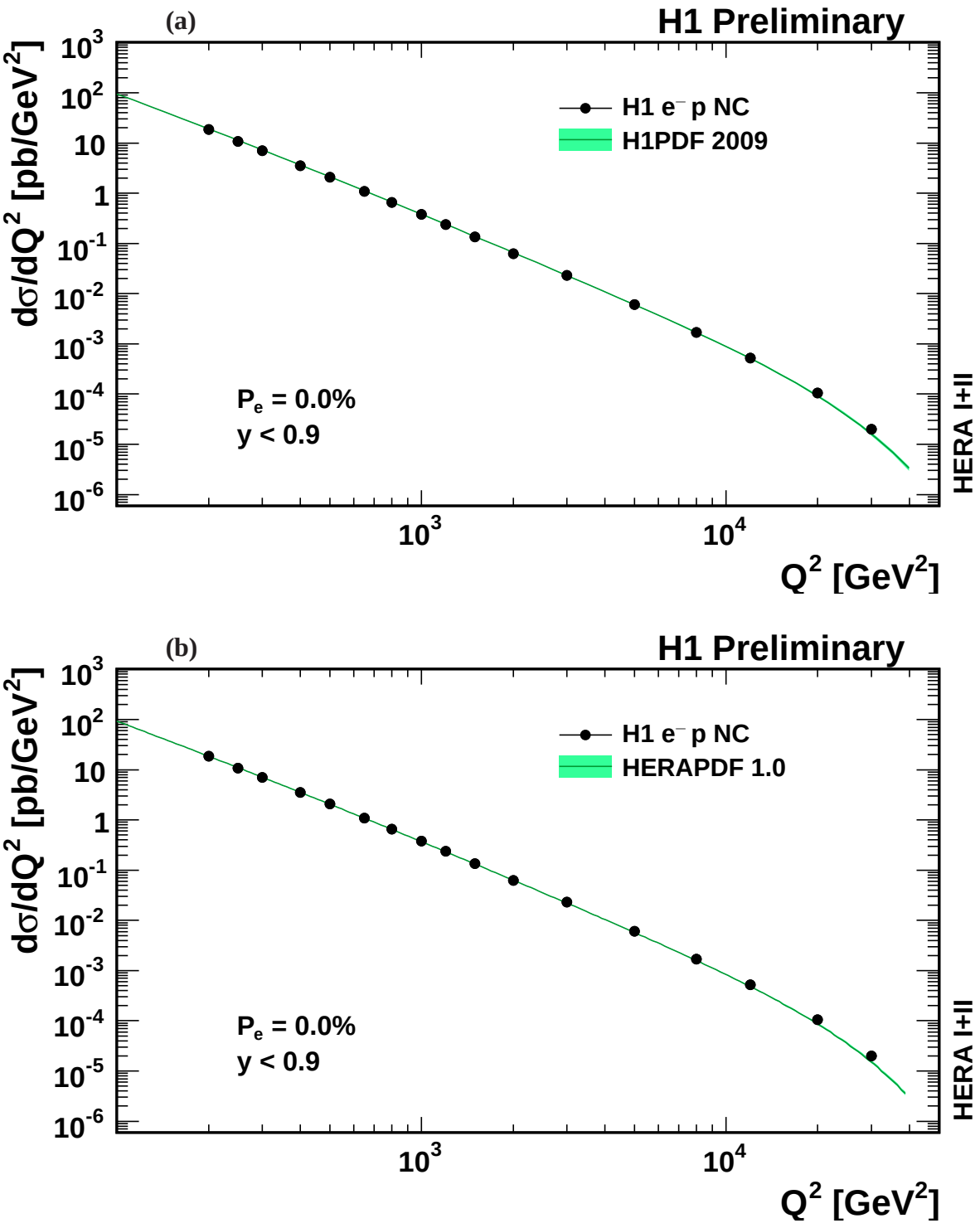


Figure 9: The $Q^2$ dependences of the unpolarised combined HERA-I+II NC cross sections $\mathrm{d}\sigma/\mathrm{d}Q^2$ for $e^-p$ scattering using PDFs obtained from (a) H1 PDF 2009 and (b) HERAPDF1.0. In addition the comparisons using CTEQ6m PDFs are also indicated. The data (solid points) are compared to the Standard Model prediction (green band). The inner error bars represent the statistical uncertainties and the outer error bars represent the total errors. The normalisation uncertainty is not included in the error bars.

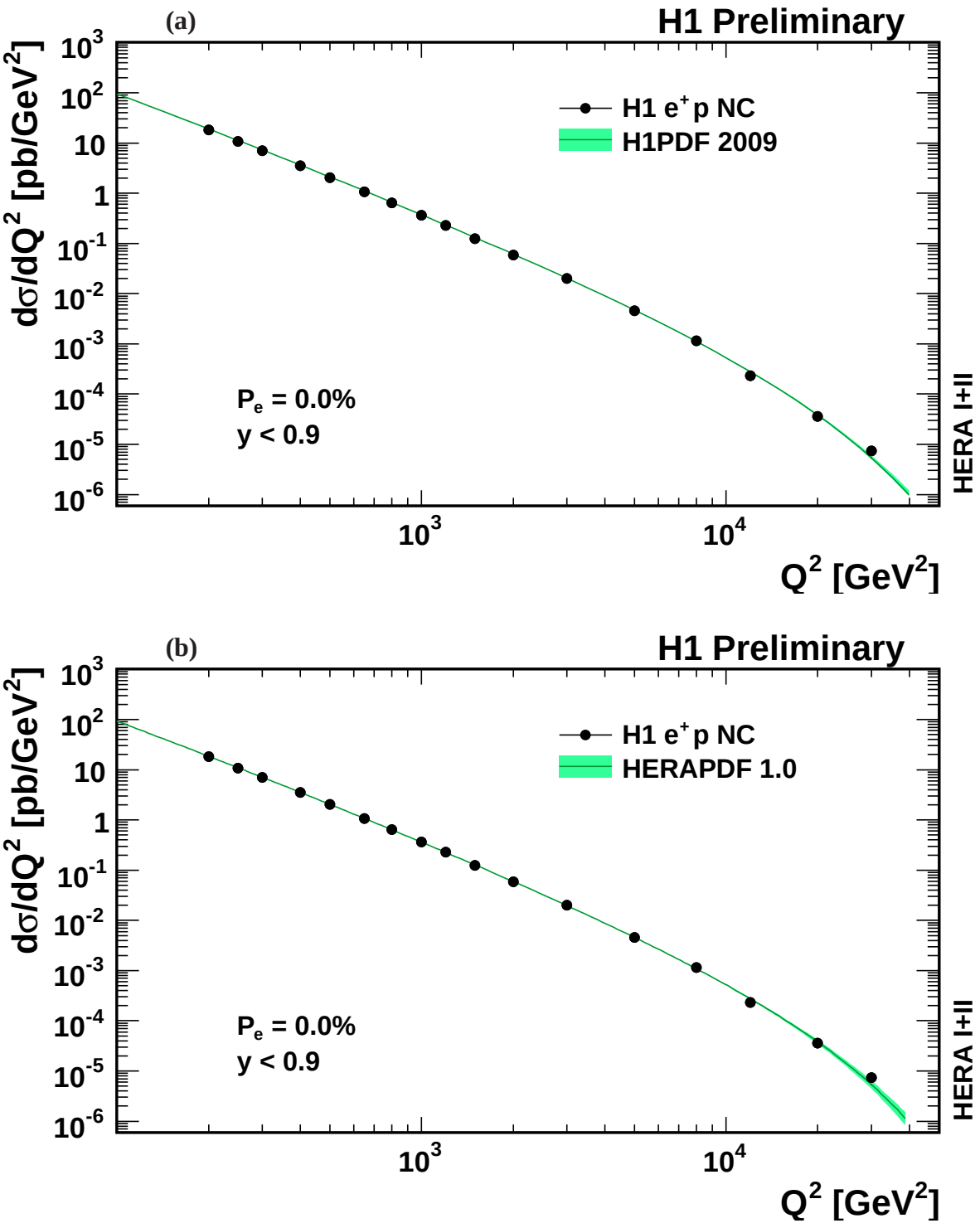


Figure 10: The $Q^2$ dependences of the unpolarised combined HERA-I+II NC cross sections $\mathrm{d}\sigma/\mathrm{d}Q^2$ for $e^+p$ scattering using PDFs obtained from (a) H1 PDF 2009 and (b) HERAPDF1.0. In addition the comparisons using CTEQ6m PDFs are also indicated. The data (solid points) are compared to the Standard Model prediction (green band). The inner error bars represent the statistical uncertainties and the outer error bars represent the total errors. The normalisation uncertainty is not included in the error bars.

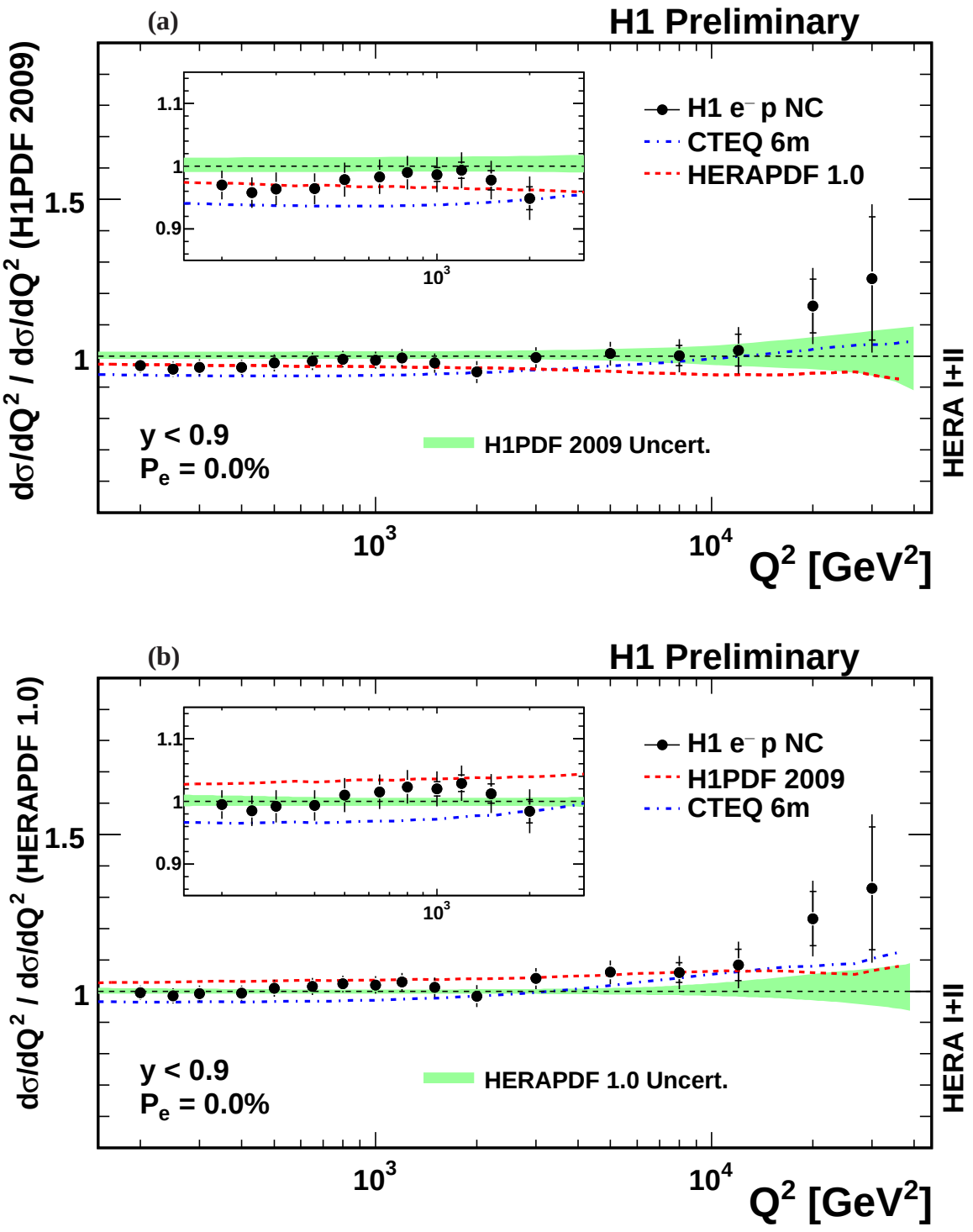


Figure 11: The $Q^2$ dependences of the unpolarised combined HERA-I+II NC cross section ratio $\mathrm{d}\sigma/\mathrm{d}Q^2$ for $e^-p$ scattering using PDFs obtained from (a) H1 PDF 2009 and (b) HERAPDF1.0. In addition the comparisons using CTEQ6m PDFs are also indicated. The data (solid points) are compared to the Standard Model prediction (green band). The inner error bars represent the statistical uncertainties and the outer error bars represent the total errors. The normalisation uncertainty is not included in the error bars and is instead represented by the blue dashed lines on the inset figures.

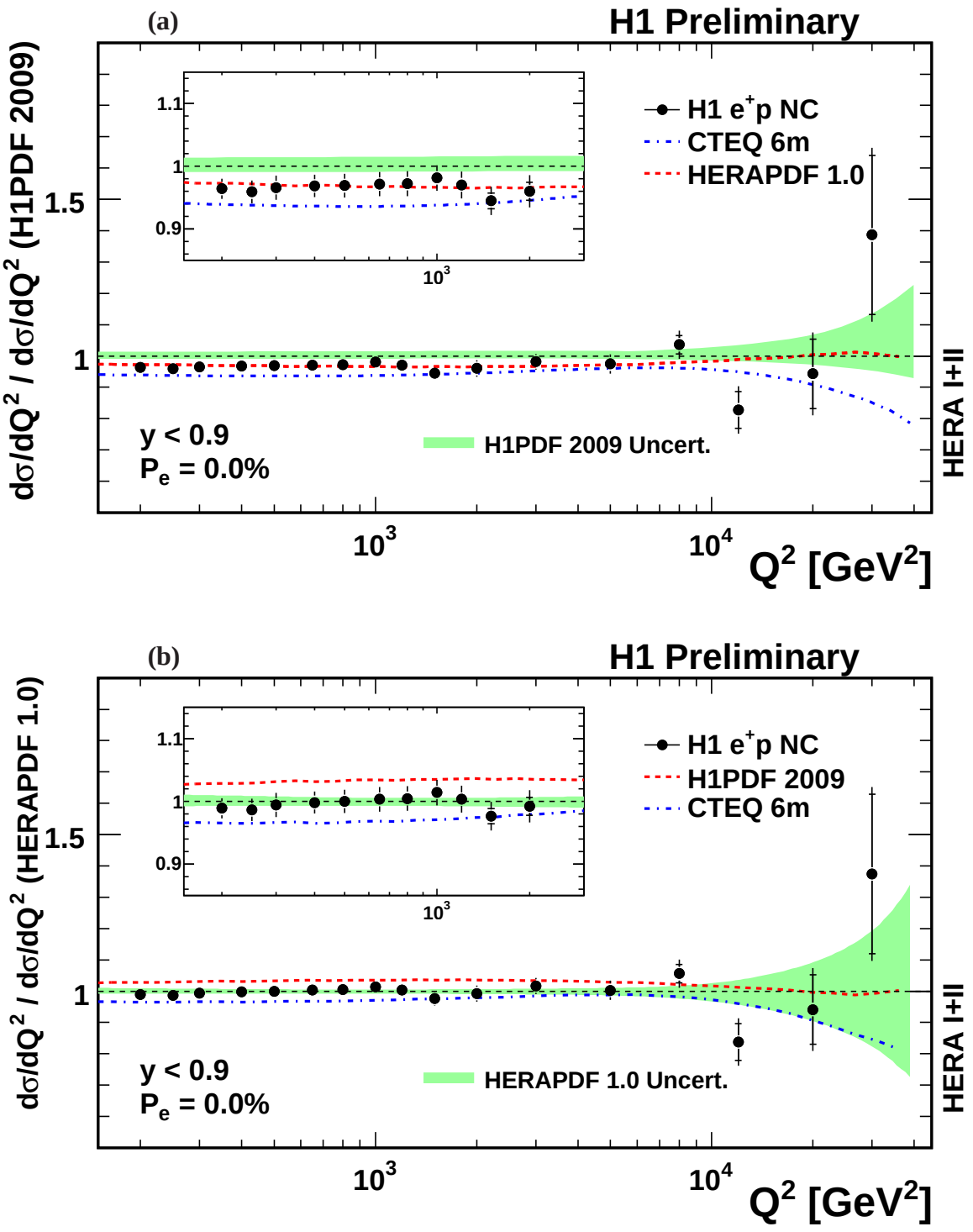


Figure 12: The $Q^2$ dependences of the unpolarised combined HERA-I+II NC cross section ratio $\mathrm{d}\sigma/\mathrm{d}Q^2$ for $e^+p$ scattering using PDFs obtained from (a) H1 PDF 2009 and (b) HERAPDF1.0. In addition the comparisons using CTEQ6m PDFs are also indicated. The data (solid points) are compared to the Standard Model prediction (green band). The inner error bars represent the statistical uncertainties and the outer error bars represent the total errors. The normalisation uncertainty is not included in the error bars and is instead represented by the blue dashed lines on the inset figures.

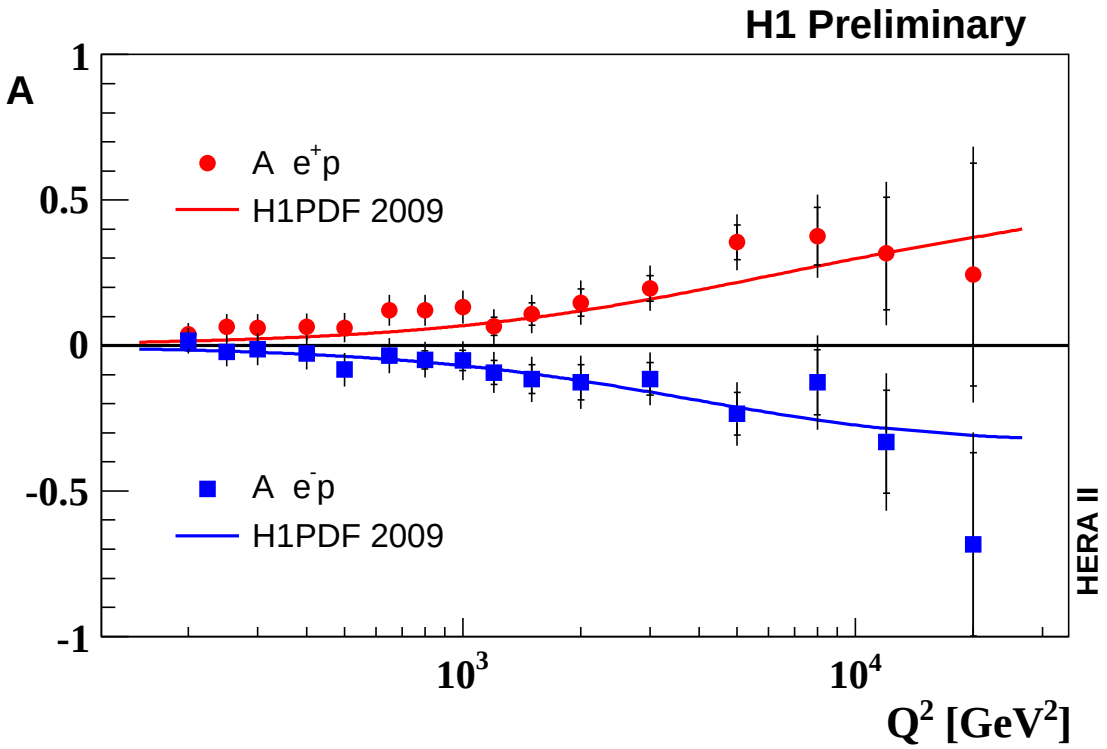


Figure 13: The $Q^2$ dependence of the polarisation asymmetry $A$, for $e^+p$ (red circles) and $e^-p$ (blue squares). The data (solid points) are compared to the Standard Model prediction (full lines). The inner error bars represent the statistical uncertainties and the outer error bars represent the total errors. The normalisation uncertainty is not included in the error bars.

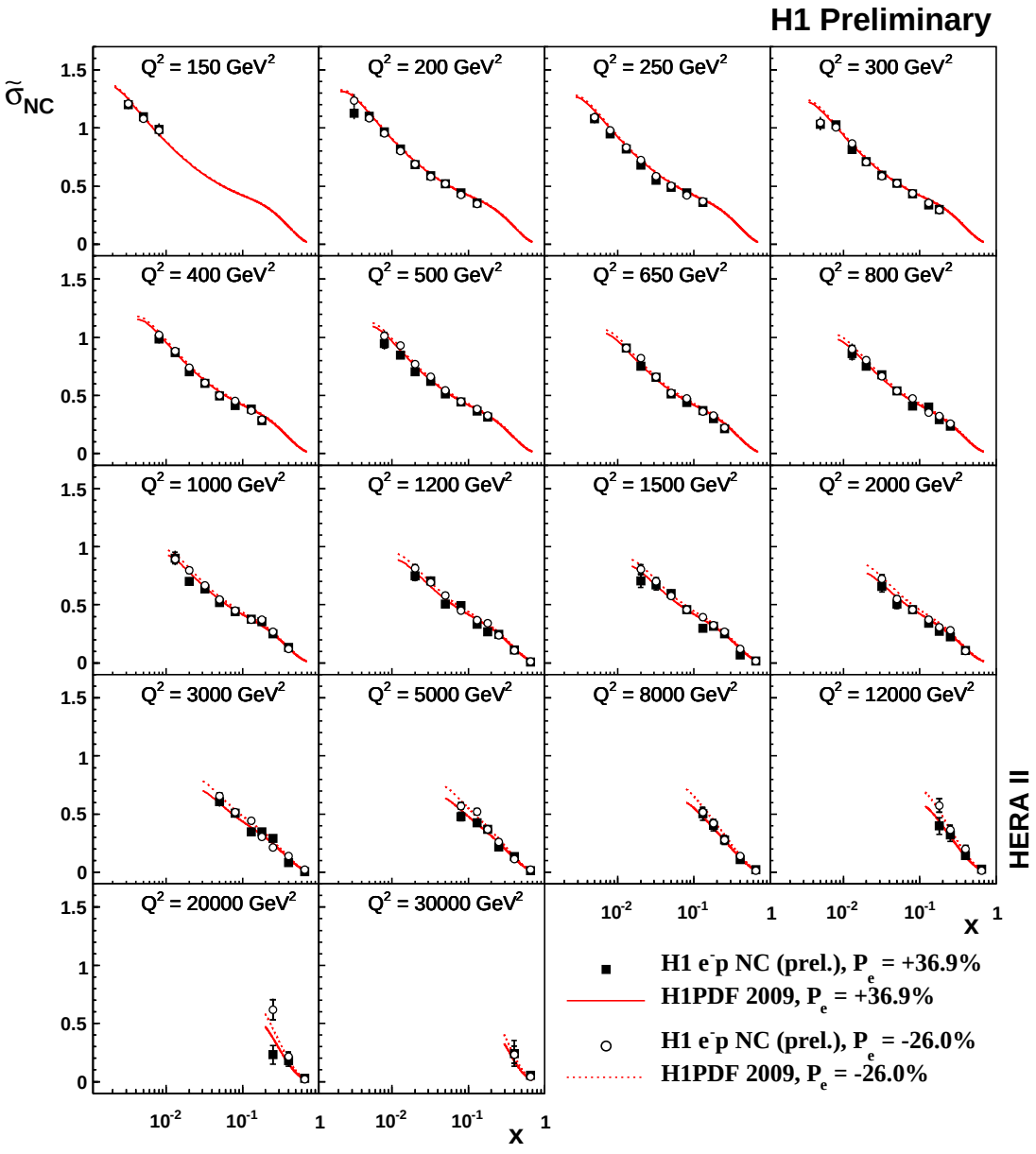


Figure 14: The reduced cross section $\tilde{\sigma}_{NC}$ in $e^-p$ scattering for $R$ (filled sqaures) and $L$ (open circles) polarised samples. The data are compared to the Standard Model prediction from H1 PDF 2009. The inner error bars represent the statistical uncertainties and the outer error bars represent the total errors. The normalisation uncertainty is not included in the error bars.

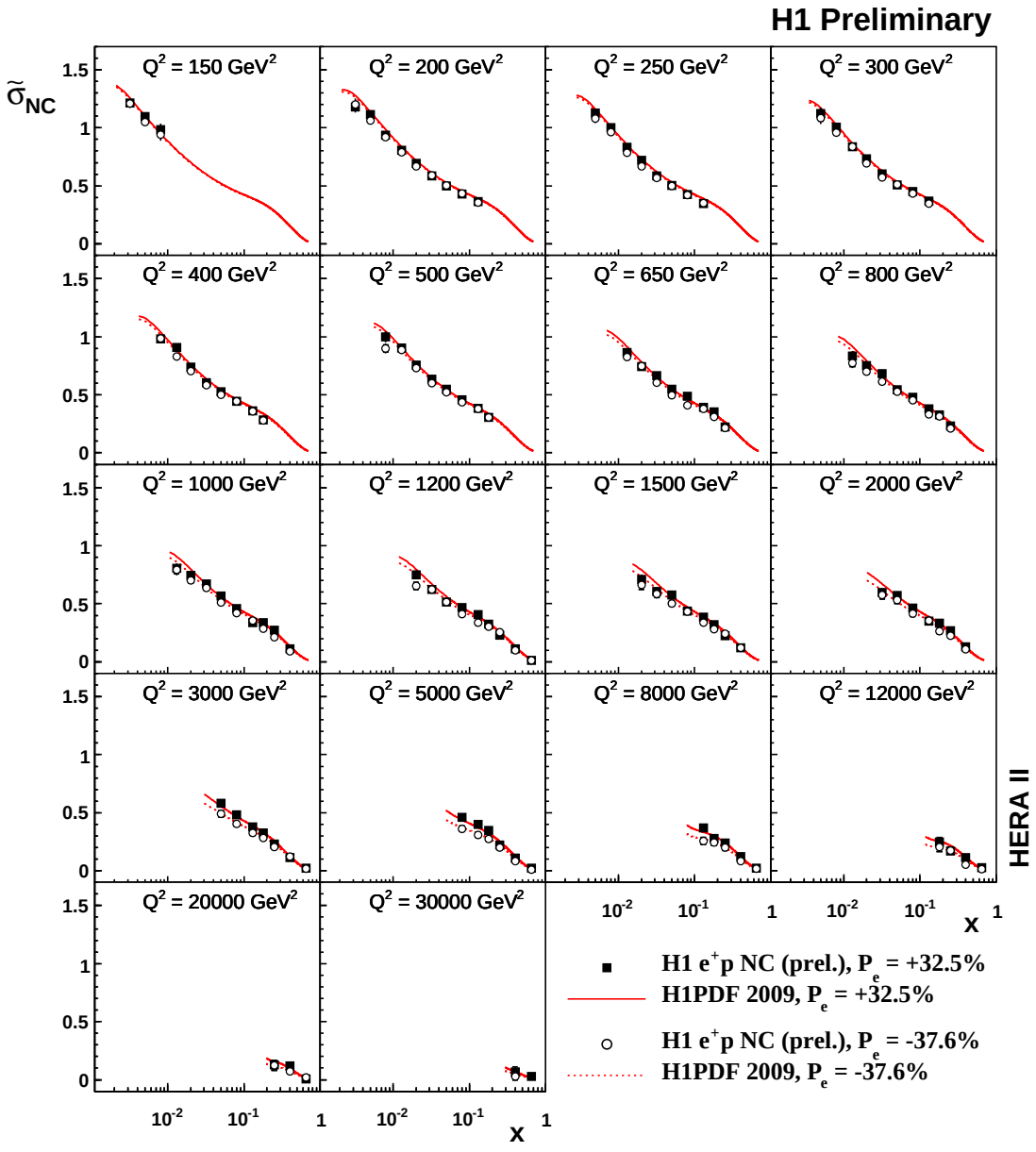


Figure 15: The reduced cross section $\tilde{\sigma}_{NC}$ in $e^+p$ scattering for $R$ (filled sqaures) and $L$ (open circles) polarised samples. The data are compared to the Standard Model prediction from H1 PDF 2009. The inner error bars represent the statistical uncertainties and the outer error bars represent the total errors. The normalisation uncertainty is not included in the error bars.

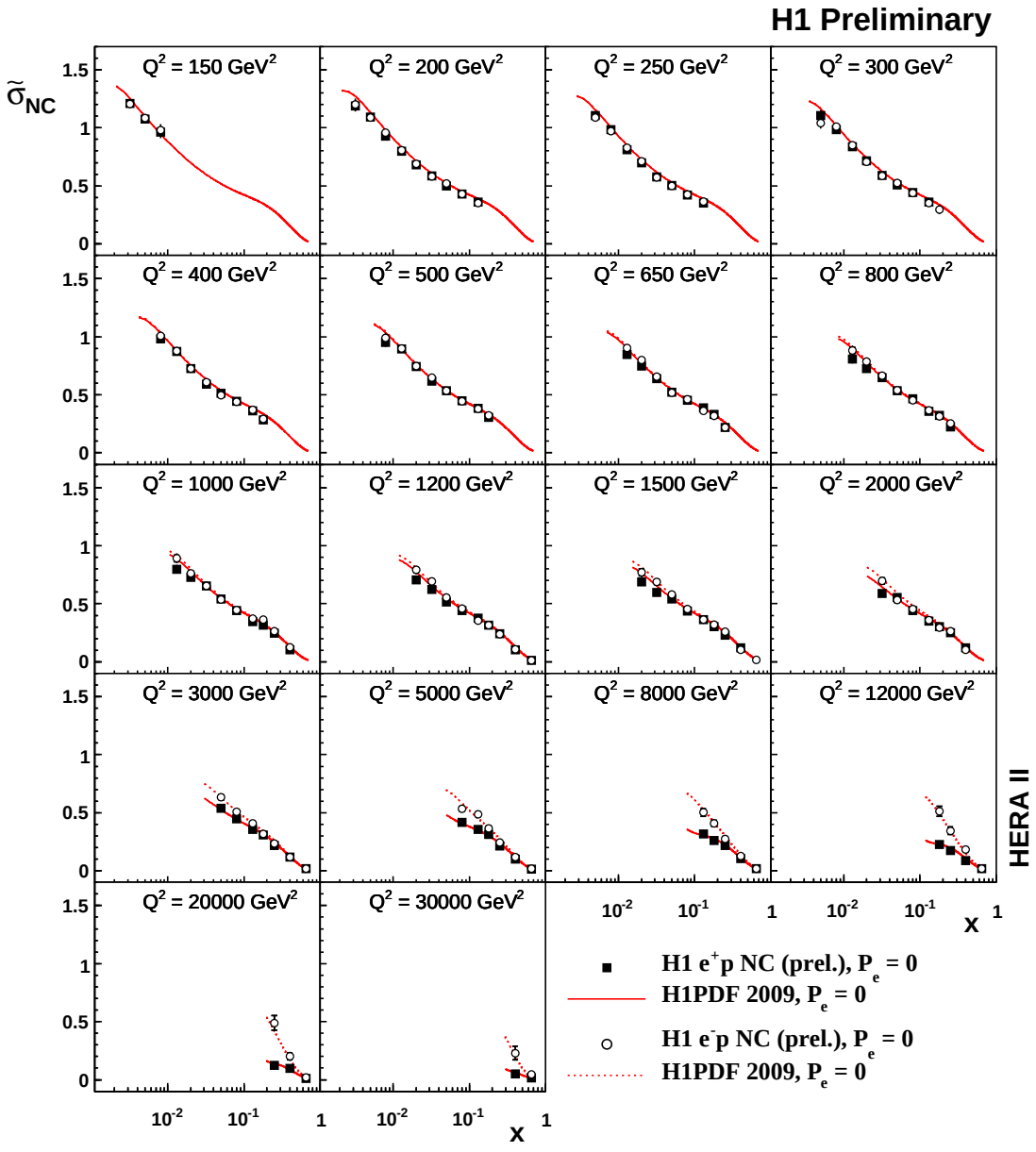


Figure 16: The reduced cross section $\tilde{\sigma}_{NC}$ in unpolarised $e^{\pm}p$ scattering. The data are compared to the Standard Model prediction from H1 PDF 2009. The inner error bars represent the statistical uncertainties and the outer error bars represent the total errors. The normalisation uncertainty is not included in the error bars.

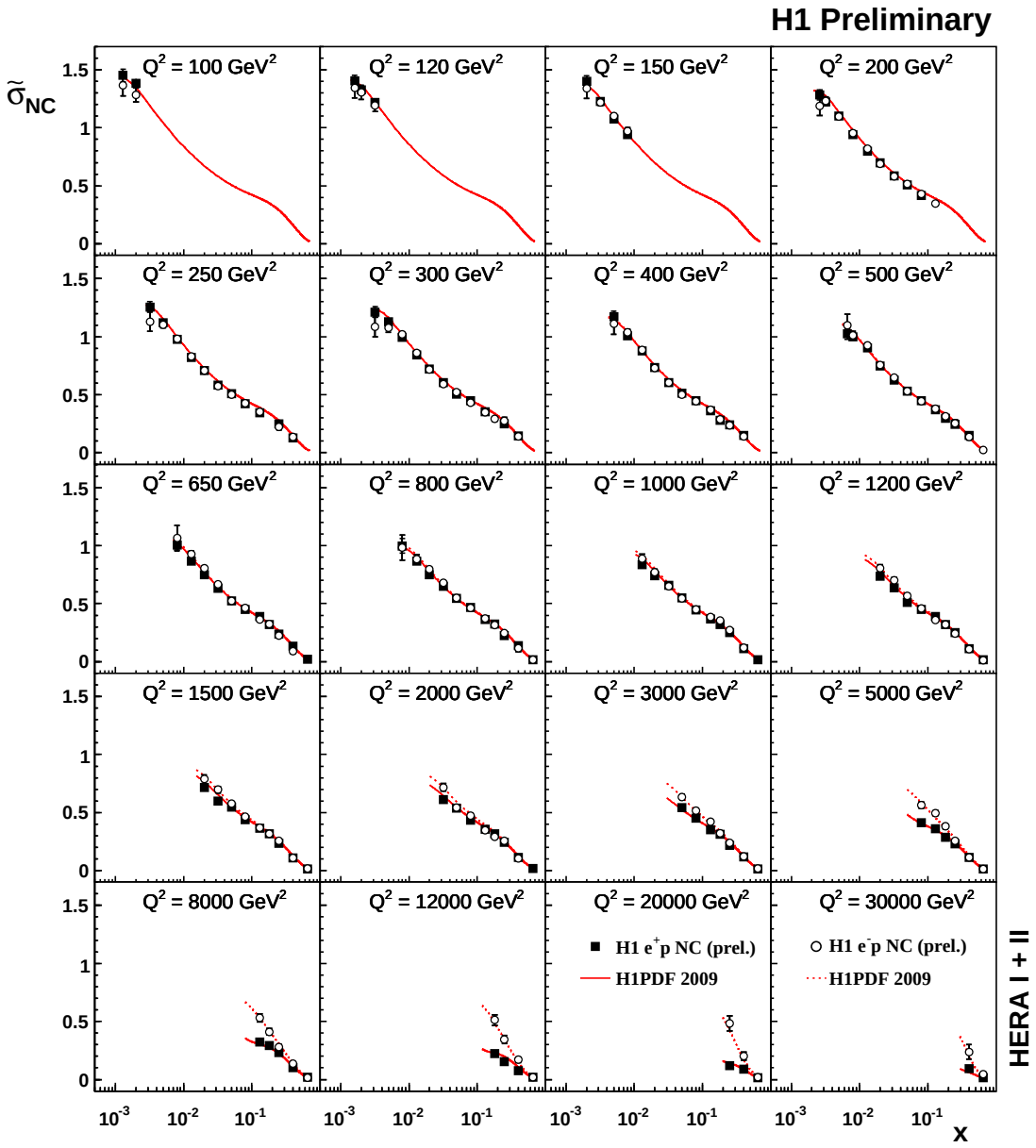


Figure 17: The reduced cross section $\tilde{\sigma}_{NC}$ in unpolarised $e^{\pm}p$ scattering using the complete HERA I+II dataset. The data are compared to the Standard Model prediction from H1 PDF 2009. The inner error bars represent the statistical uncertainties and the outer error bars represent the total errors. The normalisation uncertainty is not included in the error bars.

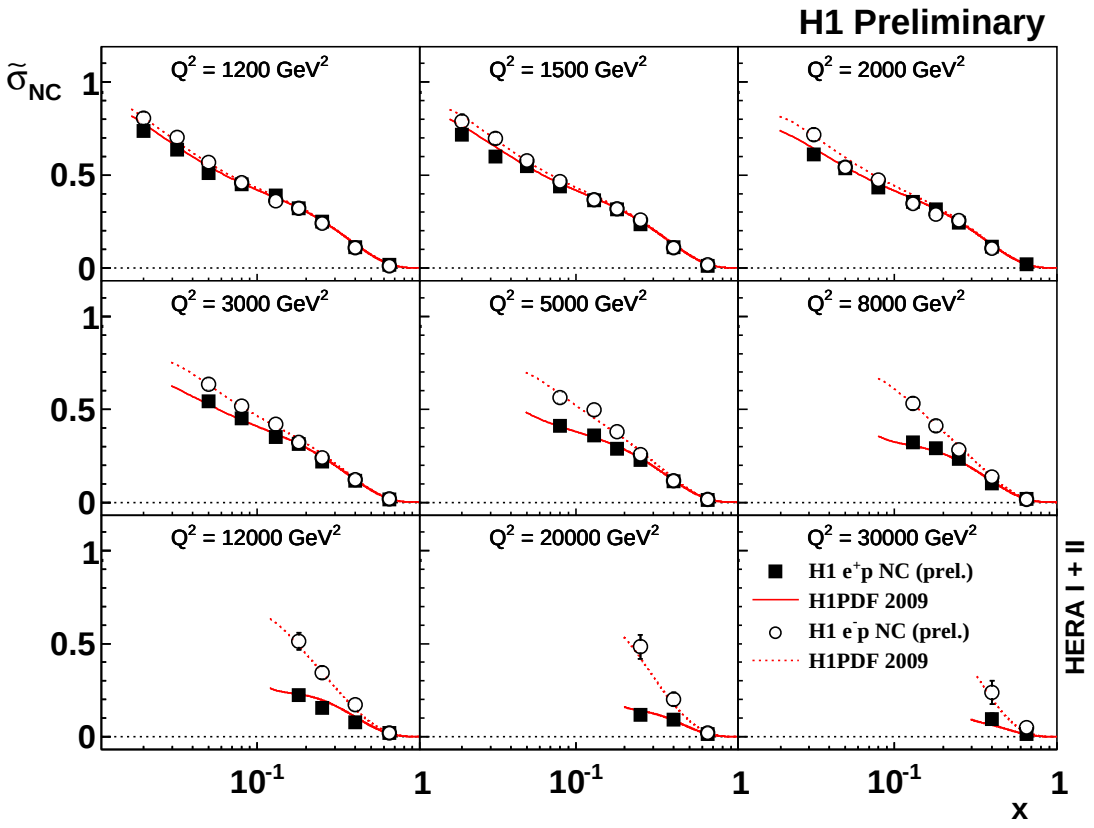


Figure 18: The reduced cross section $\tilde{\sigma}_{NC}$ in unpolarised $e^{\pm}p$ scattering using the complete HERA I+II dataset for $Q^2$ above $1\,000$ GeV$^2$. The data are compared to the Standard Model prediction from H1 PDF 2009. The inner error bars represent the statistical uncertainties and the outer error bars represent the total errors. The normalisation uncertainty is not included in the error bars.

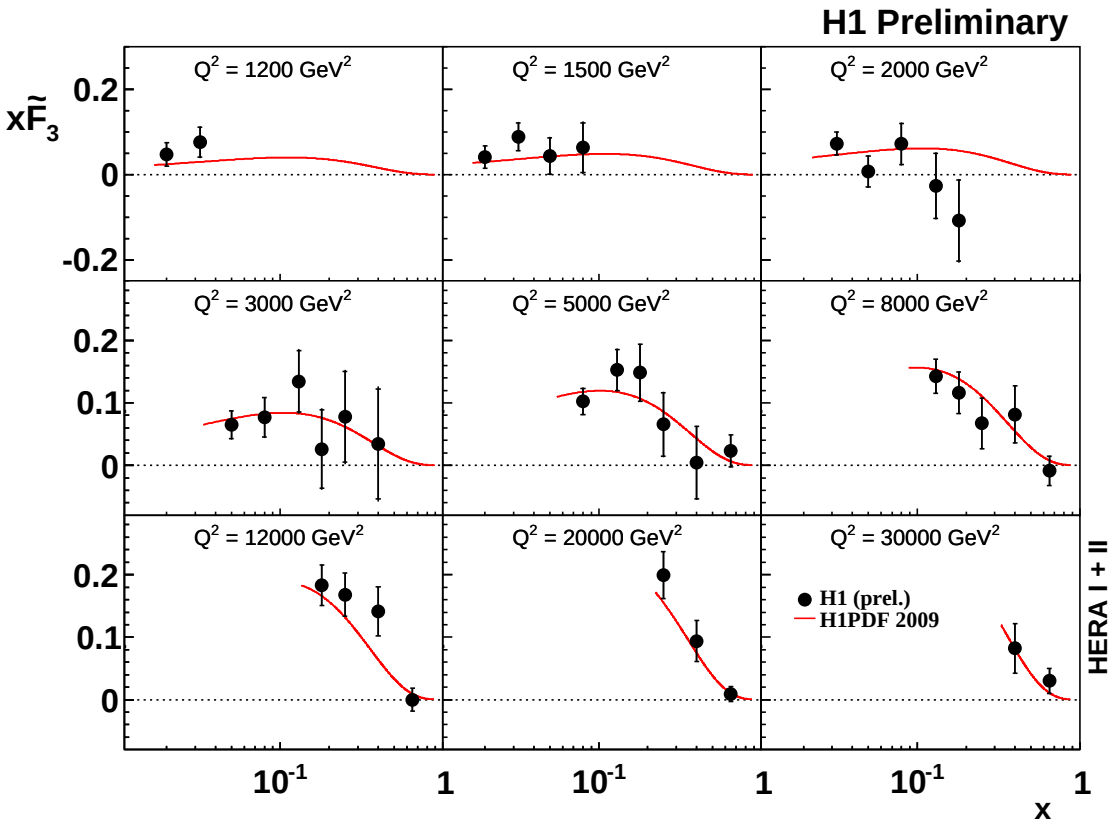


Figure 19: The structure function $x\tilde{F}_3$ evaluated using HERA-I and HERA-II data is shown (solid points) compared to the Standard Model expecation from H1 PDF 2009(solid curve). The inner error bars represent the statistical uncertainties and the outer error bars represent the total errors which includes the normalisation uncertainty.

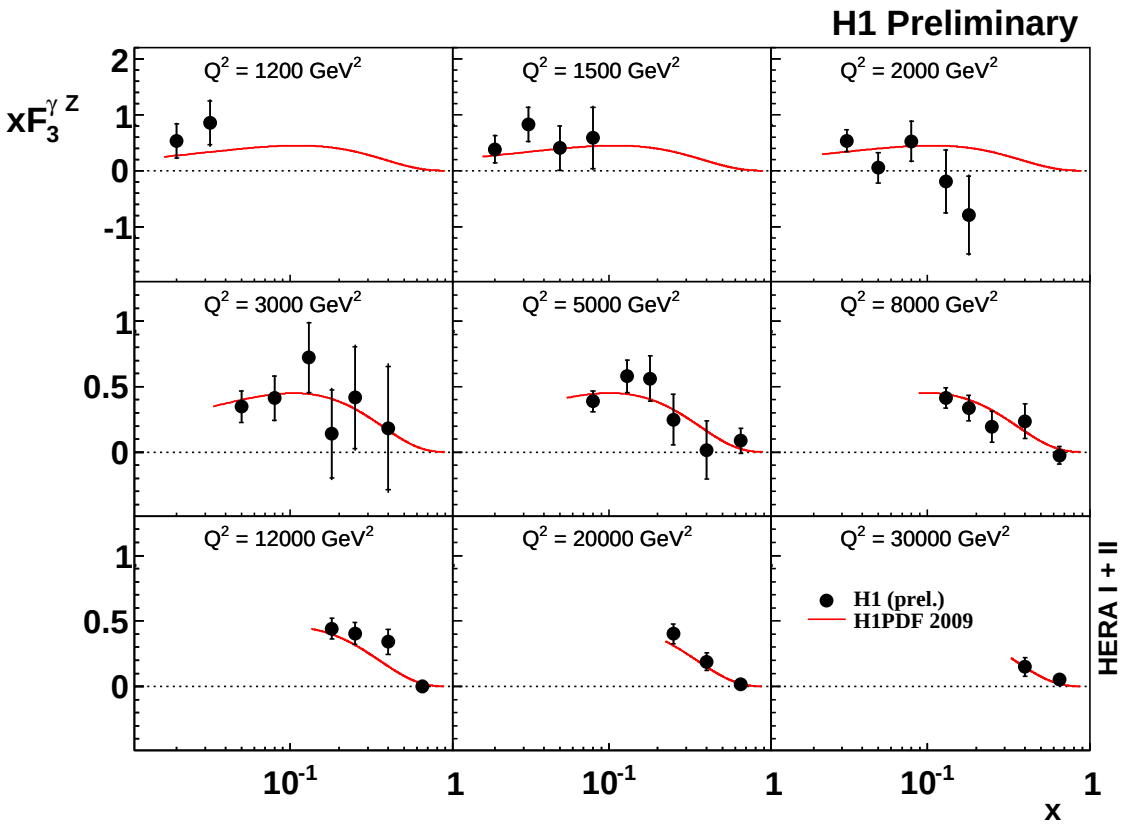


Figure 20: The structure function $xF_3^{\gamma Z}$ extracted from all HERA-I and HERA-II data (solid points) is shown together with the Standard Model expectation from H1 PDF 2009 (solid curve). The inner error bars represent the statistical uncertainties and the outer error bars represent the total errors which includes the normalisation uncertainty.

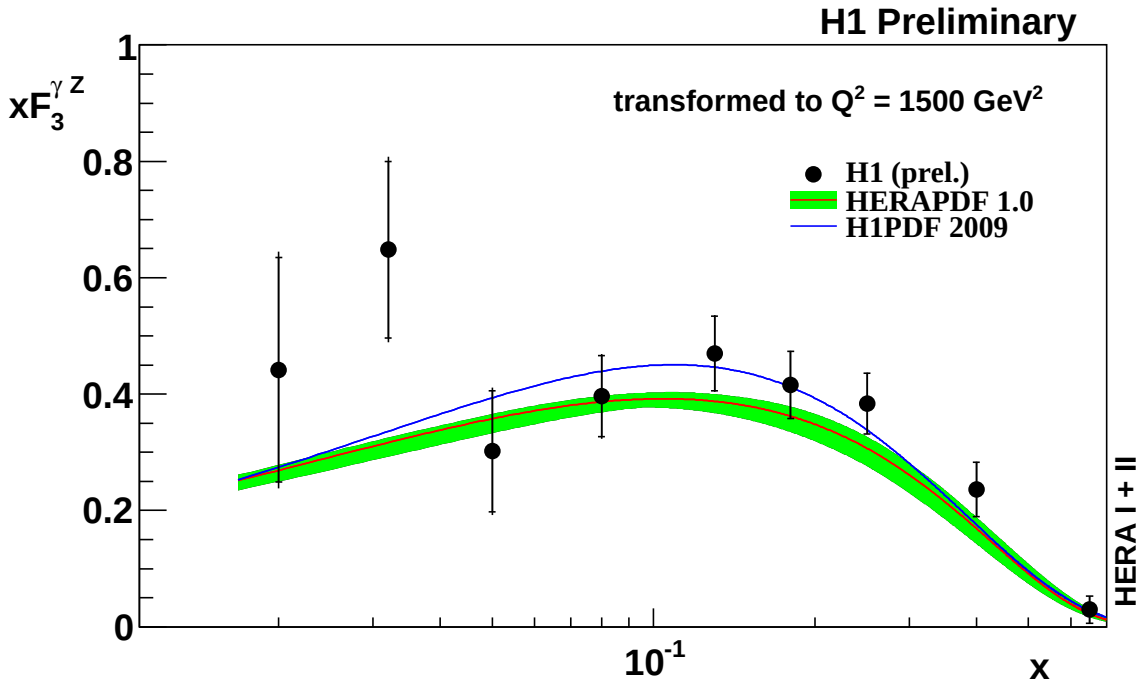


Figure 21: The structure function $xF_3^{\gamma Z}$ extracted from all HERA-I and HERA-II data (solid points) and transformed to $Q^2 = 1\,500\,\mathrm{GeV}^2$ is shown together with the Standard Model expectation from H1 PDF 2009 (solid curve) and HERAPDF 1.0 (shaded band). The inner error bars represent the statistical uncertainties and the outer error bars represent the total errors which includes the normalisation uncertainty.